Photoinduced currents and inverse Faraday effect in graphene quantum dots

Zi-Yang Xu [1] and Hang Xie [1,2,*]

[1]*College of Physics, Chongqing University, Chongqing 401331, China*
[2]*Chongqing Key Laboratory for Strongly-Coupled Physics, Chongqing University, Chongqing 401331, China*

In this work, we employ the quantum perturbation theory to investigate the photoinduced currents in graphene quantum dots (GQDs). We find that under the radiation of circularly polarized light (CPL), two types of currents may exist. One is dynamic and oscillates along the electric field of light; the other is quasisteady, rotating around certain centers in the GQD. The rotational currents can generate a magnetic moment, an effect known as the inverse Faraday effect. We develop a tight-binding-based perturbation theory to describe these intriguing and novel currents in GQDs. We also analytically analyze the oscillation direction of the dynamic currents and the transfer mechanism of angular momentum in this process. We find in some nondegenerate cases the rotational photoinduced currents disappear due to symmetry breaking in the system, and the transferred angular momentum is converted into lattice chiral vibration. This research reveals the current distributions and angular momentum exchange in excited GQD systems and suggests potential applications in ultrafast magnetic memory and photodetector devices.

I. INTRODUCTION

Graphene quantum dots (GQDs) have intriguing optical properties due to their honeycomb lattice and finite-sized geometry [1,2]. Recent technological advances make specifically shaped GQDs feasible and manageable, thus they have potential applications in many fields, such as nano memory, photodetectors, and quantum computation devices [3]. Due to their shape-dependent energy levels, the absorption spectrum of GQDs can be engineered by edge types, geometric symmetry, vacancy defects, strain, and some external fields [4–7].

In the optical transition process, the selection rule is a crucial factor in determining which energy states will be excited. Typically, the selection rules impose strict transition constraints due to the conservation laws and symmetry properties of different energy states. In recent years, E. G. Kavousanaki and Y. Wang *et al.* studied the optical transitions of GQD and twisted bilayer GQD with symmetry analysis by the group theory [2,5,8]. They find irreducible representations for different symmetric states in GQD and the corresponding selection rules are proposed for linearly and circularly polarized light (CPL). In optical transitions, besides energy conservation, angular momentum conservation must also be considered. In two-dimensional materials, certain optical transition processes are closely related to the angular momentum of photons and electrons. One example is bulk MoS_2 [9]. The electron waves in the two valleys of MoS_2 have different orbital momenta. The absorbed circularly polarized photon transfers its spin angular momentum ($\hbar$) to the conduction-valley state, which has an opposite orbital angular momentum ($\hbar/2$) compared to that of the valence-valley state ($-\hbar/2$);

another example is vortex light absorption in semiconductor quantum dots [10]. The electron in a quantum dot can absorb both the orbital and spin angular momenta of the vortex light, thereby changing its orbital angular momentum.

When a beam of CPL is incident on a GQD, the angular momentum absorbed by the electrons can generate circular currents, inducing a magnetic field and magnetic moment [8]. This photoinduced magnetization is known as the inverse Faraday effect (IFE) [11,12]. Not only the CPL with the spin angular momentum, but the vortex light with the orbital angular momentum can also induce IFE [12,13]. The traditional IFE is often focused on the charged particles in plasma and electrons in metallic materials [14–16], and it is described by the classical Drude model [11,17]. Recently, researchers have proposed quantum theories of IFE for graphene, Weyl semimetals, and other systems [18,19]. I. D. Tokman *et al.* found that the IFE strength is much stronger in Dirac materials than in common semiconductors. Using chiral plasmonic antenna structures, researchers found that the IFE can exist in only one helicity of CPL [15]. S. O. Potashin *et al.* also studied the hydrodynamic IFE of nanospheres embedded in electron liquids [20]. The IFE in Mott insulators is also studied with the Floquet theory [21]. Researchers found that with or without inversion symmetry, the photoinduced magnetization can couple neighboring spins with ferromagnetic or antiferromagnetic order. In fact, IFE is a second-order nonlinear optical effect. The optical rectification effect induced by CPL generates optomagnetics [22].

Although there is extensive research on symmetry-related optical transitions in GQDs and other graphene systems [23], and the IFE has been intensively studied in many materials, there are few detailed investigations on photoinduced currents and IFE-related magnetizations in GQDs. Especially, the optical current distributions in different GQDs have not

---

*Contact author: xiehang2001@hotmail.com

been reported, as to our knowledge. The study for the transfer mechanism of the angular momentum under CPL on GQD is also lacking.

In this paper, we use the tight-binding model and time-dependent perturbation theory to investigate photoinduced currents in GQDs and analyze the detailed process of angular momentum transfer in different shapes of GQDs. We find that two types of currents exist in irradiated GQD. One oscillates in the same direction as CPL, while the other type is quasisteady and rotates around some center(s) in GQD. The latter undergoes the transferred angular momentum from the absorbed CPL. We also find that in the symmetry-broken GQD, there is only a nondegenerate excitation level. In that case, the IFE for the excited electron is suppressed, and the dynamic current exhibits some special behavior. Due to the conservation law of angular momentum, the angular momentum in the absorbed photons will be transferred into the lattice chiral vibration or chiral phonons through the electron-lattice coupling [24,25].

This work is organized into three parts. Section II gives the main models and the theory of GQD under the CPL radiation. Section III shows our calculation results and detailed discussions, especially the mechanism of the angular momentum transfer. Section IV is the conclusion. Additional derivation details are included in the Appendices.

II. MODEL AND THEORY

A. Tight-binding model

In this work, we employ the tight-binding (TB) model to describe the electron states in the GQD. In each carbon atom, we only consider the p_z orbital to construct the molecular orbitals and the nearest-neighboring approximation is used. The Hamiltonian in this TB model is given as follows [8,26]:

$$H_0 = -t \sum_{\langle i,j \rangle} \hat{c}_i^\dagger \hat{c}_j, \tag{1}$$

where $\hat{c}_i^\dagger$ and $\hat{c}_i$ are the creation and annihilation operators for an electron at the atomic orbital with index i; in the summation, $\langle i, j \rangle$ denotes that i and j atoms are nearest neighbors; t is the hopping energy which is $t = 2.7$ eV for GQD [27,28]; When diagonalizing this Hamiltonian in the N atomic basis, we obtain the eigenenergy E_k and the corresponding eigenstate with the molecular wave function $\Psi_k, k = 1, \ldots N$. In the case without any external field, all the electrons populate the molecular orbitals with the Fermi-Dirac distribution, which means they occupy the lower energy levels in priority.

B. Time-dependent perturbation theory

In the case of the external field, such as the CPL radiated on the GQD, the electrons do not obey the Fermi-Dirac distribution. We note that the GQD is positioned in the x-y plane, while the light radiates along the z axis. The Hamiltonian under this light radiation is written as

$$H = H_0 + H_{cp}(t). \tag{2}$$

Here the second term $H_{cp}(t)$ is the dipole interaction between electron and light [29,30].

$$H_{cp}(t) = -\boldsymbol{d} \cdot \boldsymbol{E}(t), \tag{3}$$

where $\boldsymbol{d} = q\boldsymbol{r}$ is the electric dipole under the light field, q is the electron charge; $\boldsymbol{r} = (x, y)$, is the electron displacement vector. The electric field of the CPL with the angular frequency ω is written as

$$\boldsymbol{E}(t) = E_0(\cos \omega t, \pm \sin \omega t), \tag{4}$$

where E_0 is the electric field and $+(-)$ denotes the left-hand (right-hand) circular polarization. Here we only consider the left-hand case, and $H_{cp}(t)$ is rewritten as

$$H_{cp}(t) = -qE_0(x \cos \omega t + y \sin \omega t). \tag{5}$$

To obtain the evolution of the electrons in these GQD under light, we use the time-dependent perturbation theory and regard the electron-light interaction term $H_{cp}(t)$ as the small perturbation. We consider the electron staying in the initial eigenstate of Ψ_k and it is induced to a series of excited states. From the perturbation scheme, the wave function under light is described as [31,32]

$$\Psi(t) = \Psi_k e^{-i\omega_k t} + \sum_{k_1} S_{k_1}(t) \langle \Psi_{k_1} | x + iy | \Psi_k \rangle \Psi_{k_1} e^{-i\omega_{k_1} t}, \tag{6a}$$

$$S_{k_1}(t) = \frac{qE_0}{2\hbar} \frac{e^{i\Delta\omega t} - 1}{\Delta\omega}, \tag{6b}$$

where $\omega_k = \frac{E_k}{\hbar}$, where E_k is the eigenenergy of the state Ψ_k, and $S_{k_1}(t)$ is denoted as the time-dependent coefficient. In the formula of $S_{k_1}(t)$, $\Delta\omega = \omega_{k_1 k} - \omega$, and $\omega_{k_1 k} = \omega_{k_1} - \omega_k$. We here employ the rotating wave approximation (RWA) and only consider the first-order correction of perturbation. The detailed derivations are given in Appendix A.

C. Photoinduced currents

Under the CPL radiation, the electron current density in this GQD is calculated by the following expression:

$$\boldsymbol{j} = \frac{q\hbar}{m} \text{Im}[\Psi^*(t) \nabla \Psi(t)]. \tag{7}$$

Here $\boldsymbol{j}$ is the current density vector and m is the electron mass. Substituting Eq. (6a) into Eq. (7), we could obtain three types of current densities ($\boldsymbol{j}_{\text{type-I}}, \boldsymbol{j}_{\text{type-II}}, \boldsymbol{j}_{\text{type-III}}$), which are as follows:

$$\boldsymbol{j} = \boldsymbol{j}_{\text{type-I}} + \boldsymbol{j}_{\text{type-II}} + \boldsymbol{j}_{\text{type-III}}, \tag{8a}$$

$$\boldsymbol{j}_{\text{type-I}} = \frac{q\hbar}{m} \text{Im}(\Psi_k^* \nabla \Psi_k) = 0, \tag{8b}$$

$$\boldsymbol{j}_{\text{type-II}} = \frac{q\hbar}{m} \text{Im} \sum_{k_1} \left(G_{k_1} \Psi_k^* \nabla \Psi_{k_1} + G_{k_1}^* \Psi_{k_1}^* \nabla \Psi_k \right), \tag{8c}$$

$$\boldsymbol{j}_{\text{type-III}} = \frac{q\hbar}{m} \text{Im} \sum_{k_1 k_2} G_{k_1}^* G_{k_2} \Psi_{k_1}^* \nabla \Psi_{k_2}, \tag{8d}$$

where $G_{k_1} = S_{k_1}(t) \langle \Psi_{k_1} | x + iy | \Psi_k \rangle e^{-i\omega_{k_1} t}$.

Equation (8b) tells the first type of current is zero, for the fact that in the absence of optical perturbation, the ground

state corresponds to zero photoinduced current. It should be noted that the type-I current may not be always zero if some other representation is utilized. For instance, considering the discrete rotational symmetry of GQDs, we can obtain Kramers doublets in some GQDs, which do exhibit two intrinsic type-I currents with the same magnitude but opposite directions [2,8]. In our work, we are primarily concerned with the photoinduced current.

In the absorption spectra calculation [see Eq. (10)], significant transitions only occur under the Fermi golden rule, which means $\Delta\omega$ approaches zero, i.e., $\omega = \omega_{k_1 k} = \omega_{k_2 k}$. Therefore, we rewrite Eq. (8d) as

$$\boldsymbol{j}_{\text{type-III}} = \frac{q\hbar}{m} \text{Im} \sum_{k_1 k_2} |S(t)|^2 \langle \Psi_{k_1} | x - iy | \Psi_k \rangle$$
$$\times \langle \Psi_{k_2} | x + iy | \Psi_k \rangle \Psi_{k_1}^* \nabla \Psi_{k_2}. \tag{8e}$$

Here $S(t) = S_{k_1}(t) = S_{k_2}(t)$.

In the long-time case, we utilize two mathematical limits $[\lim_{t\to\infty} \frac{\sin(\Delta\omega t)}{\Delta\omega} = \pi\delta(\Delta\omega), \lim_{t\to\infty} \frac{\sin^2(\Delta\omega t)}{(\Delta\omega)^2} = \pi t\delta(\Delta\omega)]$ to dismiss the $S(t)$ factor. And we use the superposition of atomic basis $|n\rangle$ to replace the molecular state $|\Psi_k\rangle$, that means $|\Psi_k\rangle = \sum_n a_n^k |n\rangle$, a_n^k is the superposition coefficient in the basis transformation, $n = 1, \ldots N$. Then we integrate $\boldsymbol{j}_{\text{type-II}}$ and $\boldsymbol{j}_{\text{type-III}}$ over the real space, and with some derivations, we obtain the final expressions of the local current on each atom n

$$\boldsymbol{J}_n^{\text{type-II}} = \frac{q^2 E_0 \pi}{m} \sum_{\langle n' \rangle} \sum_{k_1} (x_{k_1 k} \cos \omega t + y_{k_1 k} \sin \omega t)$$
$$\times (a_n^k a_{n'}^{k_1} - a_n^{k_1} a_{n'}^k) \langle n | \nabla | n' \rangle \delta(\Delta\omega), \tag{9a}$$

$$\boldsymbol{J}_n^{\text{type-III}} = \frac{q^3 E_0^2 \pi}{2m\hbar} \sum_{\langle n' \rangle} \sum_{k_1 k_2} (x_{k_1 k} y_{k_2 k} - x_{k_2 k} y_{k_1 k})$$
$$\times a_n^{k_1} a_{n'}^{k_2} \langle n | \nabla | n' \rangle t \delta(\Delta\omega), \tag{9b}$$

where $x_{k_1 k} = \langle \Psi_{k_1} | x | \Psi_k \rangle$ and $y_{k_1 k} = \langle \Psi_{k_1} | y | \Psi_k \rangle$ denote the dipole matrix elements; $\langle n' \rangle$ in the summation above means the site n' is the nearest neighbor to site n. The details are given in the Appendix B.

From Eq. (9a) we see that type-II current is dynamic, oscillating periodically with the same frequency of light. Equation (9b) shows that type-III current only exists when the excited energy levels degenerate, and it increases linearly with time. When there is no degeneracy, or $k_1 = k_2$, it is easy to see that $\boldsymbol{J}_n^{\text{type-III}}$ is zero.

D. Absorption spectrum

On the other hand, we use the Kubo formula of optical conductivity to investigate the absorption spectrum of the GQD under the CPL [2,23,33]

$$\sigma(\omega) = \frac{2\pi q^2 \omega}{A\hbar} \sum_{k_1 k} |\langle \Psi_{k_1} | x + iy | \Psi_k \rangle|^2$$
$$\times [f(E_k) - f(E_{k_1})] \delta(\Delta\omega). \tag{10a}$$

Here the Kubo formula Eq. (10a) corresponds to the type-II current, while the type-III current is considered a secondary

(nonlinear) effect. The detailed connection between type-II current and optical conductivity is presented in Appendix C.

From the spectrum, we could determine the excitation energy levels and the excitation frequency of light. In the practical calculation, we use the Lorentzian function to replace the delta function, which mimics the finite linewidth of all the GQD levels due to all the dissipations [34]

$$\sigma(\omega) = \frac{2q^2 \omega \gamma}{A} \sum_{k_1 k} |\langle \Psi_{k_1} | x + iy | \Psi_k \rangle|^2$$
$$\times \frac{f(E_k) - f(E_{k_1})}{(E_{k_1 k} - \hbar\omega)^2 + \gamma^2}. \tag{10b}$$

Here γ is the Lorentzian linewidth and A is the area of the GQD. In Eqs. (10a) and (10b), $\langle \Psi_{k_1} | x + iy | \Psi_k \rangle$ indicates under the light radiation, the electron excited from the initial state $|\Psi_k\rangle$ to the final state $|\Psi_{k_1}\rangle$, and $E_{k_1 k} = E_{k_1} - E_k$, which is the excitation energy of light between these two states. $f(E)$ is the Fermi-Dirac distribution function, and we consider the zero-temperature case. Although the absorption of these microscopic objects is very tiny, we can dissolve these quantum dots in solutions and use absorption spectroscopy to measure their absorption spectra in real experiments.

It is noted that all our calculations in this work are carried out in the single-electron model. No electron-electron interaction and other correlation effects are considered [35]. These effects may influence the exciton optical properties and edge magnetism of GQD [33,36], induce the spin polarizations [35]. And some quantum transport properties may also change [35]. However, under this single-electron approximation, some interesting optical excitation phenomena are found in this paper.

III. RESULTS AND DISCUSSIONS

In the following discussions, we first investigate the optical excitations of GQDs in degenerate energy levels. Then we turn to the nondegenerate levels.

There are two types of currents in the GQD in the light field. To concretely show the characteristics of these currents, we use three structures: hexagonal GQD (H-GQD), triangular GQD (T-GQD) and rectangular GQD (R-GQD). The H-GQD, T-GQD, and R-GQD consist of 54, 33, and 66 carbon atoms, respectively, and their structures are shown in the insets of Figs. 1(a1), 1(b1), and 5(a1). These three types of GQDs have different symmetry properties and are often used in experiments [2,3,37]. Moreover, by introducing H-GQD vacancy [shown in the insets of Fig. 5(b1)], we find that the degeneracy of excited levels has a strong effect on the light-induced currents and transfer of angular momentum from light to electron system.

A. Degenerate energy levels

We first use the Kubo formula [Eq. (10b)] to calculate the optical absorption spectra of H-GQD and T-GQD, as shown in Figs. 1(a1) and 1(b1). The approximate Lorentzian linewidth γ in the Kubo formula is set to $0.02t$ (0.054 eV). The light energy for the absorption peaks in the absorption spectrum corresponds to the resonance to CPL. We are primarily
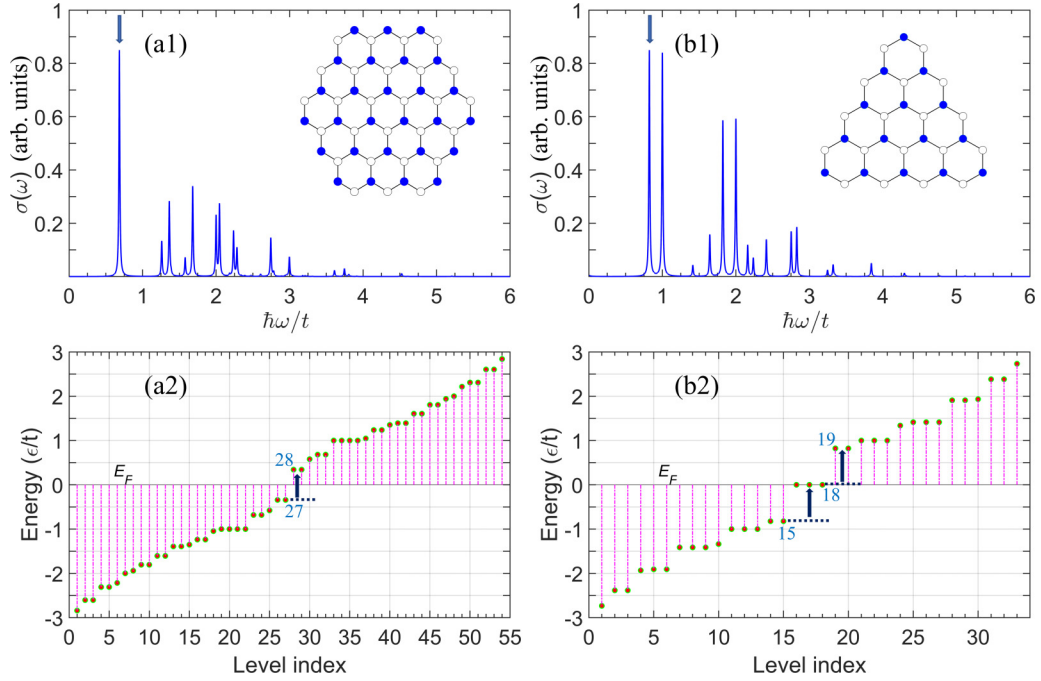
FIG. 1. Absorption spectra (upper panels) and energy spectra (lower panels) for GQD. Panels (a1) and (a2) correspond to H-GQD and panels (b1) and (b2) correspond to T-GQD respectively. In (a1) and (b1), the insets are the shapes of the GQDs, and the arrowed absorption peaks correspond to the electron transitions in (a2) and (b2). In (a2) and (b2), the arrows indicate the optical transitions between the two sets of degeneracy energy levels with some indexed numbers.

interested in the absorption peaks at the lowest frequency. In Fig. 1(a1), the absorption peak indicated by the arrow has a frequency of $0.684t$ (1.847 eV), while in Fig. 1(b1), the absorption peak indicated by the arrow has a frequency of $0.823t$ (2.222 eV).

Figures 1(a2) and 1(b2) depict the energy spectra of H-GQD and T-GQD, respectively with the tight-bonding model. We see that these spectra exhibit some degenerate energy levels. The Fermi level (E_F), which is defined at zero energy, is occupied by half of the electrons in T-GQD. For H-GQD, there is a band gap of $0.684t$ (1.847 eV). And the arrowed absorption peak of H-GQD in Fig. 1(a1) corresponds to the transitions between the energy levels with the indices $26, 27 \rightarrow 28, 29$, as indicated by the arrow in Fig. 1(a2). The excited levels 28 and 29 are degenerate in energy. Similarly, in Fig. 1(b1), the arrowed absorption peak of T-GQD corresponds to the two types of transitions: one is between the energy level indices $14, 15 \rightarrow 16, 17, 18$ and the other is between the level induces $16, 17, 18 \rightarrow 19, 20$, as indicated by the arrows in Fig. 1(b2). These excited levels are also degenerate.

Through spectroscopic and energy analysis, we focus on the absorption peaks and their corresponding transitions indicated by the arrows in Fig. 1. Therefore, under the CPL at this frequency, using the time-dependent perturbation theory [Eqs. (6a) and (9)], we can determine the wave functions and calculate the photoinduced currents (type-II and type-III). To better illustrate the current characteristics, we choose H-GQD as an example to show these currents in detail.

The Type-II currents vary dynamically with the rotational electric field of light. For a clear demonstration, we assume that H-GQD is radiated by CPL at the specified frequency

as arrowed in Fig. 1. The calculated type-II currents in this H-GQD are shown in Fig. 2, where Figs. 2(a)–2(f) depict the snapshots of current distributions at different times within one period T. We observe that these dynamic currents rotate at the same frequency as the incident light. At any time, its average vector direction aligns with the electric field direction of light. The relationship between them is described by $\boldsymbol{J} = \sigma \cdot \boldsymbol{E}$, where σ is the electrical conductivity. We see that here σ can
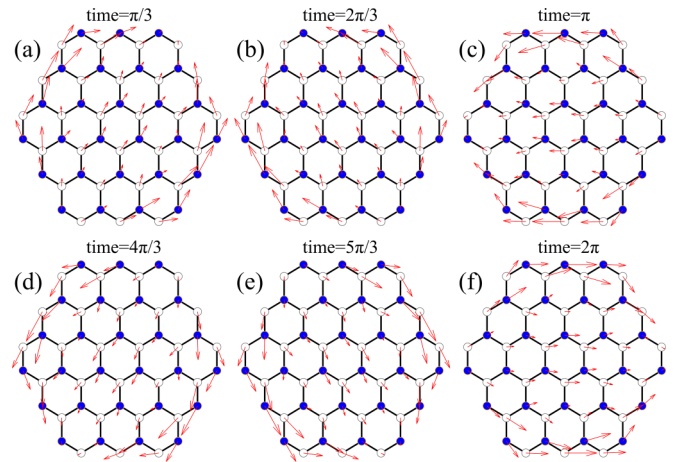

FIG. 2. The dynamic type-II local current distributions in the H-GQD under the CPL. Panels (a)–(f) are snapshots in the period of light with the time (in unit $\frac{T}{2\pi}$) of $\frac{\pi}{3}$, $\frac{2\pi}{3}$, π, $\frac{4\pi}{3}$, $\frac{5\pi}{3}$, and 2π, respectively. The transition energy corresponds to the arrowed peak in Fig. 1(a2).
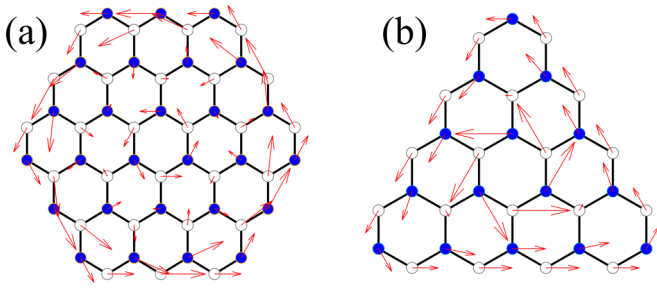
FIG. 3. The type-III steady local current distributions in H-GQD and T-GQD under CPL. The transition energy corresponds to the arrowed peaks in Figs. 1(a2) and 1(b2).

be regarded as a scalar, due to the symmetric geometry of the H-GQD.

Using a similar methodology, we can obtain the type-II current distribution of T-GQD in the corresponding transition frequency (see Fig. 1). It shows the same dynamic variations as H-GQD, although the results and analysis are not presented here.

Besides the type-II currents in GQDs, type-III currents are also found to exist in H-GQD and T-GQD, due to the degeneracy of excited levels. These type-III currents are positioned rotationally around the centers of GQDs [see Figs. 3(a) and 3(b)], which leads to the generation of a magnetic moment along the z-axis direction. We observe that type-II currents do not carry the angular momentum and magnetic moment. Based on the derivation in Sec. II, the type-III currents actually have a small fluctuation with a very low frequency, due to the fact that the real energy level has some linewidth broadening and the experimental frequency mismatch. But there still exist the average net magnetic moments in the radiation process. So, we can conclude that when electrons in GQDs undergo optical transitions, they can effectively absorb the angular momentum of light and may subsequently generate quasisteady rotational currents. An interesting observation in this work is that the transfer of angular momentum between light and electrons depends on the degeneracy of excitation levels.

In our TB model, the highest occupied molecular orbital (HOMO) levels in some GQDs may also be degenerate [see Figs. 1(a2) and 1(b2)]. In that case, the electrons in these degenerate states are considered to be uncorrelated. Therefore, we only need to calculate the photoinduced currents (type-II and type-III) generated from the transition in each single HOMO state and summate all the currents as the final results.

To better demonstrate the findings, in this work we focus on the very small GQDs, whose eigenvalues are easily distinguishable. For the much larger-sized GQD, which is more realistic in experiments, our theory can also be used. And the photoinduced current can be converted into macroscopic dynamic or quasisteady currents through the integration of type-II and type-III currents within atoms in a specific region. However, in the large-sized GQD, the photoinduced currents may be on the boundaries of GQD if the lowest unoccupied molecular orbital (LUMO) and HOMO energies are close to the Fermi level. We note that the total current vector is always in the same direction as the electric field of the CPL.

In Appendix D, we present the current distributions for two types of larger-sized GQDs.

We emphasize that the type-III rotational current does not necessarily rotate around the center of the GQD. Actually, the excited magnetic moments may also rotate around the corners of T-GQD. This finding is detailed in Appendix E.

Now we know the apparent characteristics of type-II and type-III local currents. However, the formation reason of type-III currents remains unclear. To further investigate this reason and the angular momentum transfer mechanism, we calculate the charge density variations at different times, compared to the electric field directions of the CPL. They are shown in Figs. 4(a)–4(f). The charge density variations are compared with the background of the charge in the nonradiation case. From Figs. 4(a)–4(f), we observed that the charge density variation rotates with time. Furthermore, it is clear that throughout one period, the phase of the polarization vector always lags behind that of the electric field, with a stable phase difference of about 90°.

According to the optical torque in the polarized media [38],

$$M = \frac{dL}{dt} = P \times E, \tag{11}$$

we know that the charge polarization P and electric field E in a medium may generate some torque M, as long as P and E are not in the same direction. L is the angular momentum. This indicates that in the case of degeneracy of excitation levels, CPL radiation not only induces a quasielectric-potential, but also exerts a torque on the charges in GQD. This torque makes the formation of Type-III current, enabling the transfer of angular momentum between light and electrons in GQDs. A more detailed discussion of the torque exerted on other GQDs will be presented in Fig. 8 later.

B. Nondegenerate energy levels

Besides the photoinduced currents in GQD with degenerate excited states, in this section, we will study the photoinduced currents and angular momentum transfer in nondegenerate cases. This nondegenerate energy state is illustrated using two types of GQDs. One is the R-GQD that has lower structural symmetry and nondegeneracy levels; and the other is the vacancy-structured hexagonal-GQD (VH-GQD), which presents a broken symmetry and transforms the degenerate energy levels into nondegenerate states. From the group theory, the degeneracy of the GQD orbitals also corresponds to the symmetry of the system (or its Hamiltonian). It may be related to the dimensionality of the corresponding irreducible representation of the symmetry group [39]. For example, in R-GQD, the dimensionality of all the irreducible matrices is 1 [2], so all their eigenvalues are nondegenerate.

Under the radiation of CPL, the optical absorption spectra of R-GQD and VH-GQD are shown in Figs. 5(a1) and 5(b1). Here we continue to focus on the absorption peak at the low-frequency position.

For R-GQD, we choose the second absorption peak (indicated by the arrow), which arises from the transitions between the levels (indexed 32 and 35) near the Fermi surface. In Fig. 5(a1), the absorption peak has a frequency of $0.482t$ eV. For VH-GQD, the frequency of the absorption peak indicated
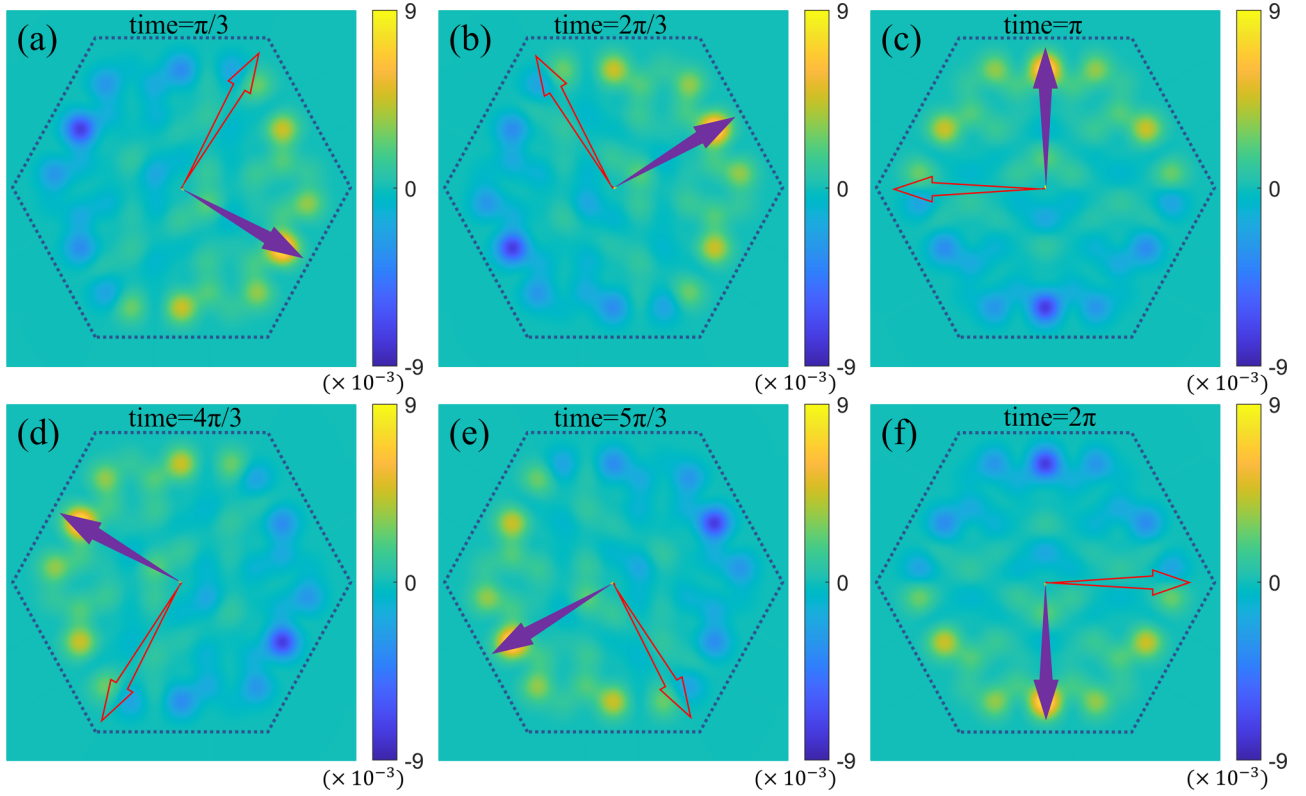
FIG. 4. The electric charge density variation distributions of H-GQD under the light radiation. [(a)–(f)] Different times (in unit $\frac{T}{2\pi}$) in one period of light, which correspond to the times in Fig. 2. The red hollow arrows represent the electric-field direction of light at that time, while the purple-filled arrows represent the charge polarization direction.
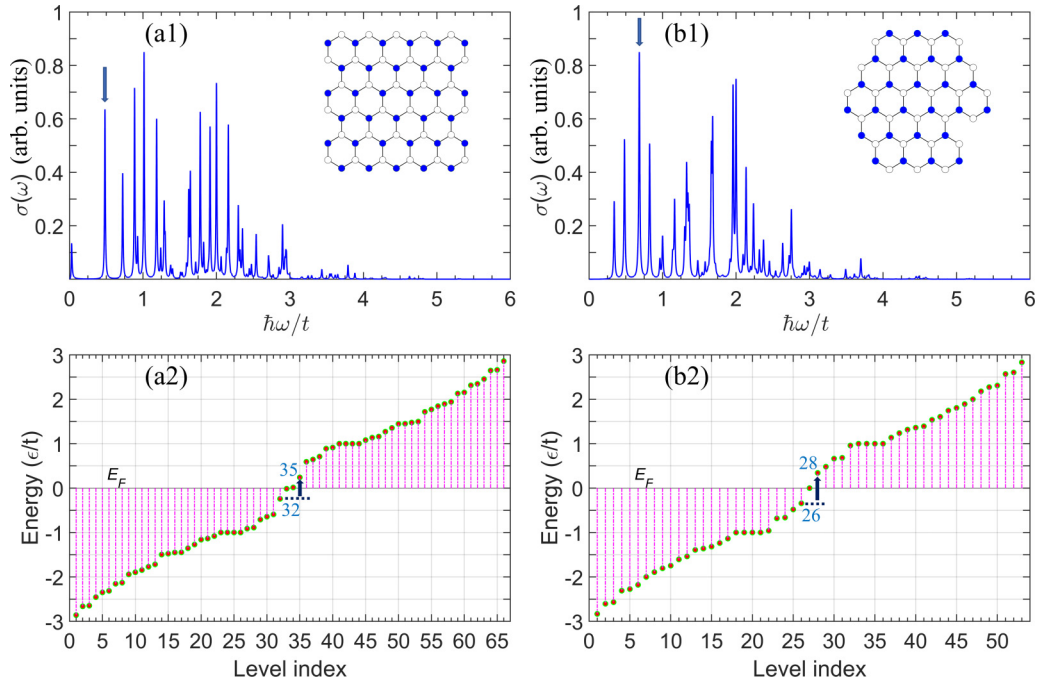

FIG. 5. Absorption spectra (upper panels) and energy spectra (lower panels) for R-GQD and VH-GQD. (a1) and (a2) correspond to R-GQD; and (b1) and (b2) correspond to VH-GQD, respectively. In (a1) and (b1), the insets are the shapes of the GQDs, and the arrowed absorption peaks correspond to the electron transitions in (a2) and (b2). The two sets of nondegeneracy energy levels in the optical transitions by arrows are indexed in (a2) and (b2).
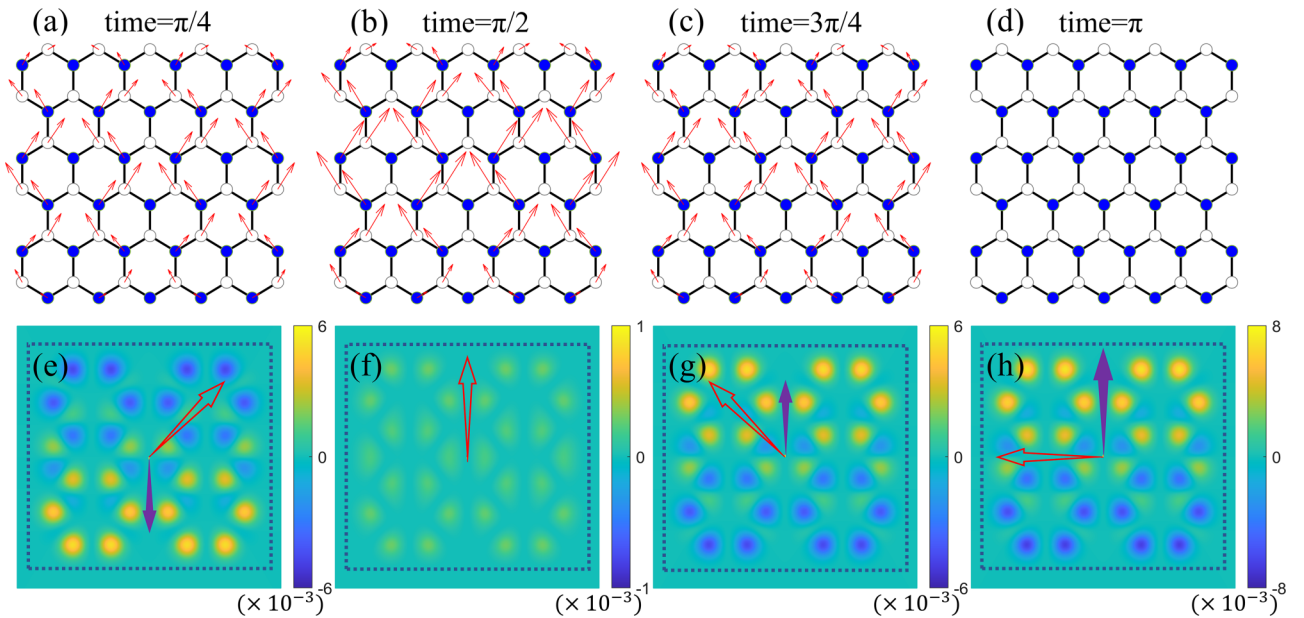
FIG. 6. The distributions of dynamic Type-II local currents and electric charge density variations of R-GQD under the CPL. The transition energy corresponds to the arrowed peak in Fig. 5(a2). [(a)–(h)] Snapshots in a half period of light with different times (in $\frac{T}{2\pi}$ unit) of $\frac{\pi}{4}$ [(a) and (e)], $\frac{\pi}{2}$ [(b) and (f)], $\frac{3\pi}{4}$ [(c) and (g)], and π [(d) and (h)]. The red hollow (purple-filled) arrows represent the electric-field vector of light (charge polarization vector) at that time.

by the arrow is also $0.684t$ eV in Fig. 5(b1), compared to H-GQD.

Figures 5(a2) and 5(b2) show that the energy levels near the Fermi energy are not degenerate. The arrows in Figs. 5(a1) and 5(a2) indicate the electrons in R-GQD transit from the energy levels indices $32 \rightarrow 35$, and for VH-GQD the electrons transit from the energy level indices $26 \rightarrow 28$.

For these two GQD systems, we utilize the time-dependent perturbation theory to obtain the photoexcited currents. We find that for these nondegenerate transitions, only type-II currents exist; while the type-III currents do not exist, as stated in Sec. II. The resulting local current variations are shown in Figs. 6 and 7.

1. Photoinduced currents in R-GQD

Figure 6 shows the snapshots of type-II current and differential charge density distributions under the CPL radiation as H-GQD. Only half of the period is shown here, and the distributions in another half period are in opposite directions.

We see that these type-II currents [Figs. 6(a)–6(d)] still vary with the change of electric field of light with the same frequency. But different from the rational current directions in H-GQD, the local current vectors at each atom only oscillate along some specific direction. We observe that the average vectors of these currents only lie along the y axis (as a symmetry axis). The mathematical reason for these currents will be given in Sec. III D.

Similar to the type-II currents, the charge densities of R-GQD shown in Figs. 6(e)–6(h) are polarized only in the y direction. We also see that within one period, there remains some variable phase difference between the polarization and the electric field of light. According to Eq. (11), this phase difference still generates a positive torque with the oscillating

magnitude. It is different from the degenerate transitions. We will present the details of this torque in Fig. 8.

2. Photoinduced currents in VH-GQD

We illustrate the type-II photoinduced current and charge density variation distributions of this VH-GQD under the corresponding conditions in Fig. 7. Only half period is depicted here, the current directions in the other half period are opposite. Though GQDs with regular shapes can be fabricated, there is an inevitable probability of introducing vacancies for technical reasons [2,40,41]. When a vacancy exists in H-GQD, degenerate excitation levels become nondegenerate, see Figs. 5(b1) and 5(b2).

Similarly to R-GQD, the local type-II currents in VH-GQD only oscillate along specific directions. And the average currents only lie along the symmetry axis caused by the vacancy in VH-GQD, shown in Figs. 7(a)–7(d). The mathematical reason for these currents' direction will be given in Sec. III D. For the charge density variations shown in Figs. 7(e)–7(h), we see the charges are dynamically polarized only along the symmetry axis direction, resulting in the corresponding photoinduced currents flowing exclusively in this direction. There still exists some phase difference between the polarization vector and the electric field vector, which is not a fixed value and still generates a positive torque according to Eq. (11) (see details in Fig. 8).

It is noted that in these nondegenerate cases, there do not exist any type-III currents in R-GQD and VH-GQD. The reason lies in Eq. (9b) of Sec. II C.

C. Light-induced torque and magnetic moment

From Eq. (11), we can calculate the light-induced torques exerted on electrons in GQDs. Figure 8 illustrates the torques
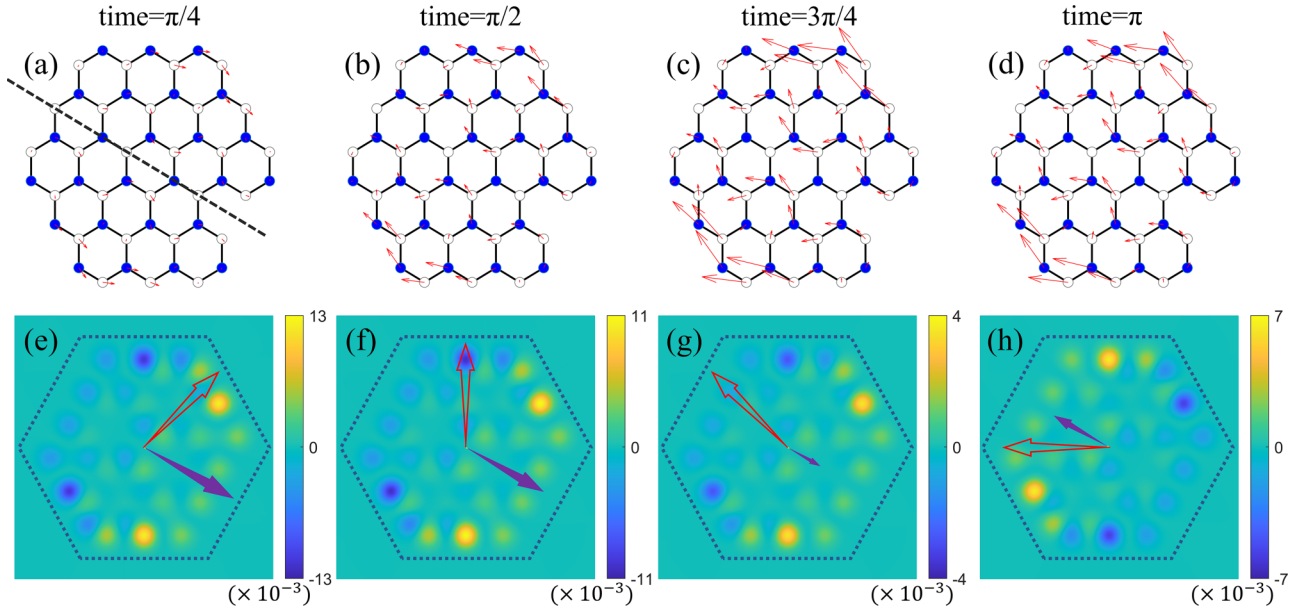
FIG. 7. The distributions of dynamic Type-II local current and electric charge density variation of VH-GQD under the CPL. The transition energy corresponds to the arrowed peak in Fig. 5(b2). [(a)–(h)] Snapshots in a half period of light with different times (in $\frac{T}{2\pi}$ unit) of $\frac{\pi}{4}$ [(a) and (e)], $\frac{\pi}{2}$ [(b) and (f)], $\frac{3\pi}{4}$ [(c) and (g)], and π [(d) and (h)]. The red hollow (purple-filled) arrows represent the electric-field vector of light (charge polarization vector) at that time. The dashed line in (a) represents the symmetry axis of this GQD.

in four types of GQDs discussed before at different times of the CPL radiation period. From this figure, we clearly observe that the torque applied to the electrons in H-GQD remains stable over one period, while in T-GQD, there is a slight fluctuation. On the other hand, for R-GQD and VH-GQD the magnitude of the torque exerted on the electrons undergoes harmonic oscillation between zero and its maximum value, with a period of half of the light period.

We now further analyze the connection between the light-induced torque and angular momentum generated by type-III rotational currents. As mentioned in the Sec. II C, Eq. (9b) shows that the type-III current is linearly related to time t. We
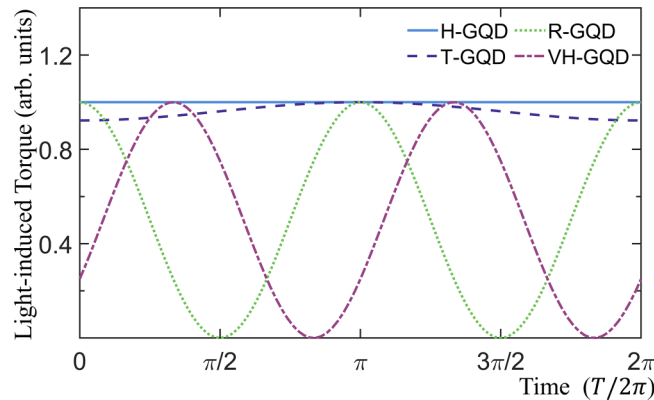

FIG. 8. Light-induced torques in one period of CPL for H-GQD, T-GQD, R-GQD, and VH-GQD. The transition energies correspond to the arrowed absorption peak in Figs. 1(a1), 1(b1), Figs. 5(a1), and 5(b1), respectively.

rewrite Eq. (9b) as

$$J_n^{\text{type-III}} = \frac{q^3 E_0^2 \pi}{2m\hbar} J_n^{\text{III}} t \delta(\Delta\omega), \tag{12}$$

where

$$J_n^{\text{III}} = \sum_{\langle n'\rangle} \sum_{k_1 k_2} \left(x_{k_1 k} y_{k_2 k} - x_{k_2 k} y_{k_1 k} \right) a_n^{k_1} a_{n'}^{k_2} \langle n|\nabla|n'\rangle.$$

We see J_n^{III} remains constant for each site of the GQD. Using the formula $\overline{j} = \eta q \overline{v}$ ($\overline{j} = J_n^{\text{type-III}}/V$, $\eta = 1/V$), where $\overline{v}$ represents velocity vector, η represents electron number density for one atom site and V is GQD volume, the photoinduced momentum of the electron on each atom site can be evaluated as

$$p_n = m v_n = m \frac{J_n^{\text{type-III}}}{q} = \frac{q^2 E_0^2 \pi}{2\hbar} J_n^{\text{III}} t \delta(\Delta\omega). \tag{13}$$

And the expression for the orbital angular momentum of the type-III currents is shown

$$L = \sum_n R_n \times p_n = \frac{q^2 E_0^2 \pi}{2\hbar} t \delta(\Delta\omega) \sum_n R_n \times J_n^{\text{III}}. \tag{14}$$

We see the orbital angular momentum of electrons in GQD also linearly increases with time (only in a proper range of time, see Appendix B), and the applied torque for generating these rotational currents is

$$M_L = \frac{dL}{dt} = \frac{q^2 E_0^2 \pi}{2\hbar} \delta(\Delta\omega) \sum_n R_n \times J_n^{\text{III}}. \tag{15}$$

Therefore, M_L is also an invariant. From the above discussions, we can conclude that the angular momentum transferred to the electrons comes from only the stable optical torque exerted on electrons of GQD. This is consistent with the results
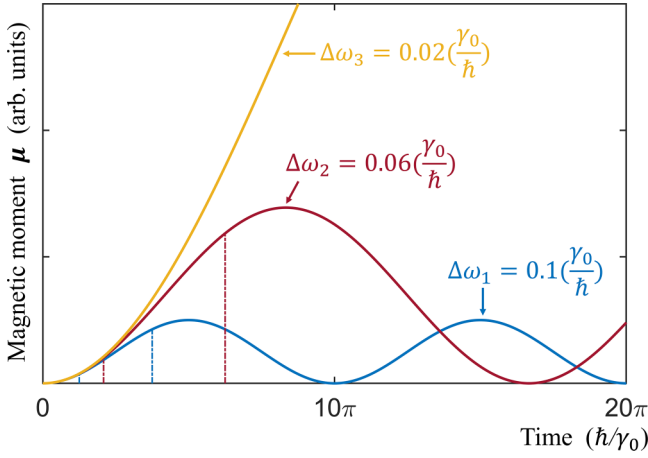
FIG. 9. The rigorous magnetic moment variations of GQD over time (in unit $\hbar/\gamma_0$), induced by three different frequency mismatches with CPL radiation. The dashed lines denote the effective time ranges that the magnetic moments have linear relations with time.

shown in Fig. 8. Only the torque variation curves of H-GQD and T-GQD are stable, and they both exhibit type-III rotating currents. On the contrary, there are no type-III currents for R-GQD and VH-GQD, so their torques have large oscillations.

Using the relationship between magnetic moment and angular momentum $\boldsymbol{\mu_L} = g_L \frac{q}{2m} \boldsymbol{L}$, where g_L is the Landé factor and for orbital motion $g_L = 1$, we have the magnetic moment generated by the type-III currents

$$\boldsymbol{\mu} = \frac{q^3 E_0^2 \pi}{4m\hbar} t\delta(\Delta\omega) \sum_n \boldsymbol{R_n} \times \boldsymbol{J_n^{III}}. \tag{16}$$

We see that under the CPL radiation, the GQD with degenerate excitation levels can become a tiny magnet. The calculated magnetic moment in Eq. (16) linearly increases with time, which is due to the ideal approximation in the long-time limit. However, there is a finite absorption linewidth γ_0 in real experiments, i.e., $\gamma_0 = \hbar\Delta\omega_0 \neq 0$. The excited magnetic moment magnitude will not continue to increase, but oscillate periodically in the long term, as shown in Fig. 9 [also see Eq. (8e)]. Here we use the rigorous expression for magnetic moment written as

$$\boldsymbol{\mu_0} = \frac{q^3 E_0^2}{4m\hbar} \frac{\sin^2(\Delta\omega t)}{(\Delta\omega)^2} \sum_n \boldsymbol{R_n} \times \boldsymbol{J_n^{III}}. \tag{17}$$

Equation (17) above is the result by removing the approximation condition $\lim_{t\to\infty} \frac{\sin^2(\Delta\omega t)}{(\Delta\omega)^2} = \pi t\delta(\Delta\omega)$, for details please refer to Appendix B. Note that only when the frequency broadening is less than the linewidth ($\Delta\omega/\Delta\omega_0 < 1$), the significant absorption or magnetic moment can exist.

Figure 9 shows the magnetic moment as a function of time for three different low-frequency mismatches ($\Delta\omega_1$, $\Delta\omega_2$, and $\Delta\omega_3$). As we see, Eq. (16) is an approximation (linear proportional to time) for the time range covered by the vertical dashed lines. On the other hand, the magnitude of this magnetic moment is still subject to the constraints of time-dependent perturbation theory, see Appendix B.

For these induced currents in the nano-sized GQD, it is difficult to detect them. However, the rotational type-III cur-

rents generate magnetic moments that are detectable using spin-polarized scanning tunneling microscopy (STM) [42,43]. Thus, we believe that our calculated photoinduced currents are experimentally measurable.

We also estimate the maximum magnetic moment generated in H-GQD and T-GQD in the case of Sec. III A. In Appendix B, it is shown that the time-dependent perturbation theory requires

$$t\delta(\Delta\omega)\frac{q^2 E_0^2 \pi}{2\hbar^2}\left(x_{k_1k}^2 + y_{k_1k}^2\right) \ll 1. \tag{18}$$

We assume

$$\max\left[t\delta(\Delta\omega)\frac{q^2 E_0^2 \pi}{2\hbar^2}\left(x_{k_1k}^2 + y_{k_1k}^2\right)\right] \approx 0.1, \tag{19}$$

$\langle n|\boldsymbol{\nabla}|n'\rangle \approx 1/\text{Å}$. By substituting the relevant data into Eq. (16), the calculated magnetic moment is approximately equal to 3.03 bohr magnetons for H-GQD and 1.42 bohr magnetons for T-GQD. However, for larger-sized GQDs, due to the increase in the number of atoms and radius, a relatively significant magnetic moment may be generated under the CPL radiation.

For the linewidth of $0.02t$ and the quantum dot size of 1 nm, we use Eq. (19) to estimate the maximum value of the electric field of light, $E_{\max} = 1.7 \times 10^7$ V/m. This field of light could be obtained by the femtosecond laser (with a pulse duration of 500 fs and peak laser pulse fluence of 0.04 mJ/cm^2). We note that with a smaller linewidth or a larger quantum size, this E-field value could be even smaller, which is more easily achieved experimentally.

D. Analysis of the direction of type-II currents

In Sec. III C, we explored the relationship between type-III rotating currents and light-induced torque, i.e., the condition for transferring the angular momentum to electrons. However, when only type-II currents exist, the torque cannot be ignored, as in the cases of R-GQD and VH-GQD shown in Fig. 8. The transferred angular momentum goes into the lattice chiral vibrations as there are no type-III currents in these nondegenerate cases. Now we focus on the type-II currents oscillations.

It can be easily observed that the periodic variations of the torque are related to the restriction of charge polarization direction (see Figs. 4, 6–8). Actually, this restriction depends on whether the excitation level is degenerate, which ultimately stems from the geometric symmetry of the system, as discussed below.

The expression for type-II currents is already written in Eq. (9a) of Sec. II C. Under the molecular basis, type-II currents can also be written as

$$\boldsymbol{J_{\text{type-II}}} = \frac{2q^2 E_0 \pi}{m} \sum_{k_1} \left(x_{k_1k}\cos\omega t + y_{k_1k}\sin\omega t\right)$$
$$\times \langle\Psi_k|\boldsymbol{\nabla}|\Psi_{k_1}\rangle\delta(\Delta\omega), \tag{20}$$

[see the derivations in Appendix B, Eq. (B6)]. Here we use the bound-state relationship: $\langle\Psi_{k_1}|\boldsymbol{\nabla}|\Psi_k\rangle = -\langle\Psi_k|\boldsymbol{\nabla}|\Psi_{k_1}\rangle$. $\boldsymbol{J_{\text{type-II}}}$ is the total vector for type-II currents.

When the excited energy level is nondegenerate, there is only one excited state Ψ_{k_1}, i.e., the summation operation in
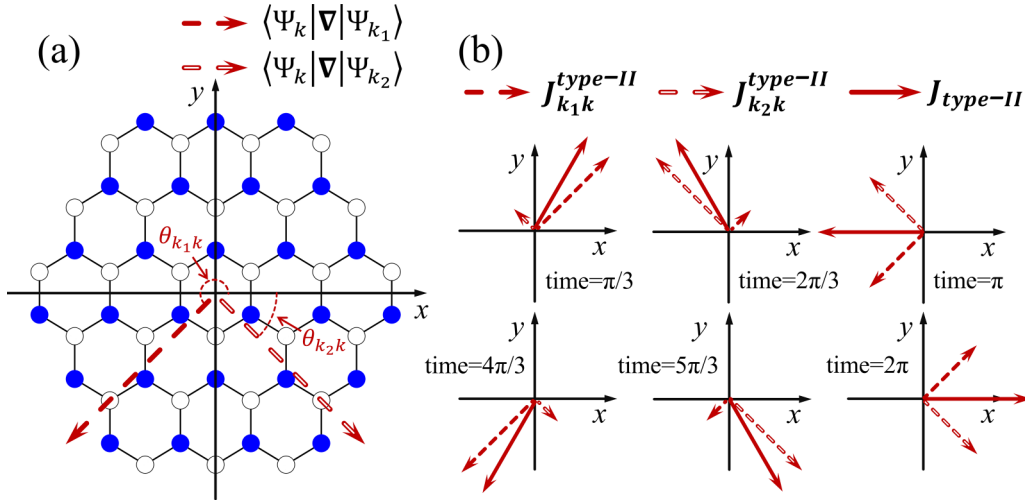
FIG. 10. (a) The inner-products directions ($\langle\Psi_k|\nabla|\Psi_{k_1}\rangle$ and $\langle\Psi_k|\nabla|\Psi_{k_2}\rangle$) for two transition modes of H-GQD ($k = 27$, $k_1 = 28$, $k_2 = 29$). (b) The corresponding type-II current vectors (transition to two single-excited states and to two degenerate states) in H-GQD under the CPL radiation for different times (in unit $\frac{T}{2\pi}$) in one period of light.

the above Eq. (20) is omitted. $J_{\text{type-II}}$ only oscillate in a fixed direction, as indicated by the vector

$$\langle\Psi_k|\nabla|\Psi_{k_1}\rangle = \left(\langle\Psi_k|\partial x|\Psi_{k_1}\rangle, \langle\Psi_k|\partial y|\Psi_{k_1}\rangle\right). \quad (21)$$

Since

$$\left(\langle\Psi_k|\partial x|\Psi_{k_1}\rangle, \langle\Psi_k|\partial y|\Psi_{k_1}\rangle\right) = \frac{m\omega}{\hbar}(x_{k_1k}, y_{k_1k}), \quad (22)$$

see Eq. (C2). We may rewrite the type-II currents as follows:

$$\begin{aligned}
J_{k_1k}^{\text{type-II}} &= \frac{2q^2 E_0 \pi \sqrt{x_{k_1k}^2 + y_{k_1k}^2}}{m} \cos\left(\omega t - \theta_{k_1k}\right) \\
&\quad \times \langle\Psi_k|\nabla|\Psi_{k_1}\rangle\delta(\Delta\omega) \\
&= \frac{2q^2 E_0 \pi \omega}{\hbar}\left(x_{k_1k}^2 + y_{k_1k}^2\right) \cos\left(\omega t - \theta_{k_1k}\right) \\
&\quad \times \left(\cos\theta_{k_1k}, \sin\theta_{k_1k}\right)\delta(\Delta\omega), \quad (23)
\end{aligned}$$

where θ_{k_1k} represents the angle between the oscillation direction determined by $\langle\Psi_k|\nabla|\Psi_{k_1}\rangle$ and the positive direction of the x axis. Equation (23) easily reveals the reason why the type-II current direction of R-GQD and VH-GQD is restricted (see Figs. 6 and 7). And $\langle\Psi_k|\nabla|\Psi_{k_1}\rangle$ (or θ_{k_1k}) ultimately depends on the geometric symmetry of the system.

When the transition levels are degenerate (at least E_{k_1}, E_{k_2} exist), $J_{\text{type-II}} = \sum_{k_1} J_{k_1k}^{\text{type-II}}$. This current is the sum of at least two vibration directions, determined by the two inner products $\langle\Psi_k|\nabla|\Psi_{k_1}\rangle$ and $\langle\Psi_k|\nabla|\Psi_{k_2}\rangle$.

Due to the orthogonality between the two eigenstates (Ψ_{k_1} and Ψ_{k_2}), the two vibration directions above must be nonparallel, i.e., they possess different phases θ_{k_1k} and θ_{k_2k} (and $|\theta_{k_1k} - \theta_{k_2k}| \neq \pi$), which form the type-II currents corresponding to the circular polarization (see Fig. 2). At the same time, there are two independent charge polarization directions, which, as a set of two-dimensional basis vectors, allows the final polarization direction to rotate with the electric field, and may generate type-III rotational currents. Thus, the symmetry-related restriction of the oscillation direction

is removed and the angular momentum transfer to electrons becomes possible.

Here we use Eqs. (20) and (23) to calculate the directions of the inner products of H-GQD for the transition modes from the energy level 27 (k) to two degenerate levels 28 (k_1) and 29 (k_2) [see Fig. 1(a2)], as shown in Fig. 10(a). The variation of the type-II current vectors $J_{k_1k}^{\text{type-II}}$, $J_{k_2k}^{\text{type-II}}$, and $J_{\text{type-II}}$ in one period are also calculated in Fig. 10(b). It can be observed that in the transition to the two single excited states, the inner products have different directions, while the overall type-II current direction rotates with the electric field. This is very similar to the formation of CPL which consists of two orthogonal electric field oscillations with different phases. This analysis is also consistent with the above simulation results.

We need to clarify that in the nondegenerate transition modes, the charge polarization direction is restricted, and it seems that the electrons do not receive angular momentum from the CPL. However, since the total angular momentum must be conserved, the angular momentum from the absorbed photons will be transferred to the lattice chiral vibration through the optical torque exerted on the GQD system by the electron-phonon interaction. In other words, the electrons in the excited energy state only serve as a medium for transferring the angular momentum, and the angular momentum carried by light will be transferred to chiral phonons [24,25,44] or even cause the overall mechanical rotation of GQDs [45–47]. Due to the much larger mass of the lattice atoms compared to the electrons, the manifestation of this effect requires a much longer calculation time and is not further analyzed in this paper.

IV. CONCLUSIONS

In this work, we use the tight-binding model and time-dependent perturbation theory to study the properties of the photoinduced currents and the mechanism of the inverse

Faraday effect in the radiated GQD systems. We find there exist two types of currents under the CPL. The first type (type-II current) oscillates with the same frequency and phase as CPL, and the polarized charge also rotates with a phase delay relative to the light. The second type (type-III current) is steady and rotates around some center(s) in GQD. This type of current is also related to the IFE and can generate magnetic moments. This rotational current results from the torque of incident CPL exerting on electron charge and is considered a second-order optical nonlinear effect.

The optical absorption spectra and photoinduced current calculations show that the degeneracy of excited states is crucial to the photoinduced currents in GQDs. The nondegenerate level often arises from the broken symmetry of GQD. In the nondegenerate-level GQD, the type-II currents do not oscillate with the same phase and direction as the CPL but only oscillate along some fixed direction. This nondegeneracy also eliminates the type-III currents, as well as the induced magnetic moments in GQD.

We further analyze the transfer mechanism of angular momentum in these radiated systems. We find that the type-II currents do not hold any angular momentum, and some of the transferred angular momentum appears in the type-III rotational currents. However, in nondegenerate GQDs, type-III currents do not exist. We consider the transferred angular momentum gained from fluctuational optical torques goes to the graphene lattices via electron-phonon coupling. This process is very similar to what happens when a beam of CPL transmits through a wire grid polarizer. The charge polarization changes only along the wire grid direction without any other vertical direction. The angular momentum conservation makes the rotation of the wire lattice in the polarizer. In our system, the nondegenerate GQD with broken symmetry acts as such a "polarizer," and the excited electrons take on the role of the angular momentum transfer from the CPL to the GQD lattice.

This paper employs some new methods to study the optical excitation process in irradiated GQDs and gives some interesting results, especially for the angular momentum transfer analysis for nondegenerate excitation systems. Further studies are also in progress, including electron-phonon interactions in irradiated GQDs and electron-photon interactions under vortex light radiation in GQD systems. We believe these novel investigations are crucial for understanding the interactions between light and quantum dots. They also have potential applications in related fields such as photon detectors and light-induced memory devices.

APPENDIX A: TIME-DEPENDENT PERTURBATION OF ELECTRON STATES

Here we derive the wave function under the CPL radiation as shown in Eq. (6a). According to the time-dependent perturbation theory, we assume the initial state is Ψ_k. In the first-order approximation of the perturbation theory, we have [32]

$$C_{k_1 k}^{(t)} = \delta_{k_1 k} + \frac{1}{i\hbar} \int_0^t e^{i\omega_{k_1 k} t'} H'_{k_1 k} dt'. \quad (A1)$$

Here $C_{k_1 k}^{(t)}$ represents the coefficient of the eigenstate Ψ_{k_1}. Note that $|C_{k_1 k}^{(t)}|^2 \ll 1$ ($k_1 \neq k$), and $H'_{k_1 k}$ is the matrix element of the perturbation $H'_{k_1 k} = \langle \Psi_{k_1} | H_{cp}(t) | \Psi_k \rangle$. Substituting Eq. (5) into this matrix element formula, we have

$$H'_{k_1 k} = -\frac{qE_0}{2} \big[\langle \Psi_{k_1} | x - iy | \Psi_k \rangle e^{i\omega t} + \text{H.c.} \big]. \quad (A2)$$

With Eq. (A2), we simplify the second term on the right side of Eq. (A1)

$$\frac{1}{i\hbar} \int_0^t e^{i\omega_{k_1 k} t'} H'_{k_1 k} dt'$$
$$= -\frac{qE_0}{2i\hbar} \bigg[\langle \Psi_{k_1} | x - iy | \Psi_k \rangle \int_0^t e^{i(\omega_{k_1 k} + \omega)t'} dt'$$
$$+ \langle \Psi_{k_1} | x + iy | \Psi_k \rangle \int_0^t e^{i(\omega_{k_1 k} - \omega)t'} dt' \bigg]. \quad (A3)$$

For visible light, the frequency ω is very large ($\omega \approx 10^{14} \sim 10^{15}$ Hz). So the RWA is used to omit the first term on the right-hand side of Eq. (A3), and then Eq. (A1) is expressed as

$$C_{k_1 k}^{(t)} = \delta_{k_1 k} + \frac{qE_0}{2\hbar} \frac{e^{i\Delta\omega t} - 1}{\Delta\omega} \langle \Psi_{k_1} | x + iy | \Psi_k \rangle. \quad (A4)$$

From Eq. (A4), we could obtain the wave function Eq. (6a) in Sec. II B from these coefficients.

APPENDIX B: DERIVATIONS OF THE LOCAL CURRENTS

Equation (8) gives the current density vectors $\boldsymbol{j}$, $\boldsymbol{j}_{\text{type-I}}$, $\boldsymbol{j}_{\text{type-II}}$, and $\boldsymbol{j}_{\text{type-III}}$ under the radiation of CPL. Here we integrate these current density vectors in the whole space to obtain the following "total" current vectors:

$$\boldsymbol{J} = \int \boldsymbol{j} d^3 \boldsymbol{r} = \boldsymbol{J}_{\text{type-I}} + \boldsymbol{J}_{\text{type-II}} + \boldsymbol{J}_{\text{type-III}}. \quad (B1)$$

Here $\boldsymbol{J}_{\text{type-I}} = 0$, and $\boldsymbol{J}_{\text{type-II}}$ and $\boldsymbol{J}_{\text{type-III}}$ are expressed as

$$\boldsymbol{J}_{\text{type-II}} = \frac{q\hbar}{m} \text{Im} \sum_{k_1} \big[S_{k_1}(t) \langle \Psi_{k_1} | x + iy | \Psi_k \rangle e^{-i\omega_{k_1 k} t} \langle \Psi_k | \boldsymbol{\nabla} | \Psi_{k_1} \rangle$$
$$+ S_{k_1}^*(t) \langle \Psi_{k_1} | x - iy | \Psi_k \rangle e^{i\omega_{k_1 k} t} \langle \Psi_{k_1} | \boldsymbol{\nabla} | \Psi_k \rangle \big], \quad (B2)$$

$$\boldsymbol{J}_{\text{type-III}} = \frac{q\hbar}{m} \text{Im} \sum_{k_1 k_2} |S(t)|^2 \langle \Psi_{k_1} | x - iy | \Psi_k \rangle$$
$$\times \langle \Psi_{k_2} | x + iy | \Psi_k \rangle \langle \Psi_{k_1} | \boldsymbol{\nabla} | \Psi_{k_2} \rangle. \quad (B3)$$

Rewrite the time-dependent factors $S_{k_1}(t)$ and $|S(t)|^2$ in Eqs. (B2) and (B3), we have the following expressions:

$$S_{k_1}(t) = \frac{qE_0}{2\hbar} \frac{e^{i\Delta\omega t} - 1}{\Delta\omega} = i\frac{qE_0}{2\hbar} \frac{\sin\left(\frac{\Delta\omega}{2}t\right)}{\frac{\Delta\omega}{2}} e^{i\frac{\Delta\omega}{2}t}, \quad \text{(B4)}$$

$$|S(t)|^2 = \frac{q^2 E_0^2}{4\hbar^2} \frac{\sin^2\left(\frac{\Delta\omega}{2}t\right)}{\left(\frac{\Delta\omega}{2}\right)^2}. \quad \text{(B5)}$$

Using two mathematical limitations: $\lim_{t\to\infty} \frac{\sin(\Delta\omega t)}{\Delta\omega} = \pi\delta(\Delta\omega)$ and $\lim_{t\to\infty} \frac{\sin^2(\Delta\omega t)}{(\Delta\omega)^2} = \pi t\delta(\Delta\omega)$, and with the Fermi-golden rule $\omega = \omega_{k_1 k} = \omega_{k_2 k}$, Eqs. (B2) and (B3) are simplified to the following form:

$$\mathbf{J}_{\text{type-II}} = \frac{q^2 E_0 \pi}{m} \sum_{k_1} \left(x_{k_1 k}\cos\omega t + y_{k_1 k}\sin\omega t\right)$$
$$\times \left(\langle\Psi_k|\mathbf{\nabla}|\Psi_{k_1}\rangle - \langle\Psi_{k_1}|\mathbf{\nabla}|\Psi_k\rangle\right)\delta(\Delta\omega), \quad \text{(B6)}$$

$$\mathbf{J}_{\text{type-III}} = \frac{q^3 E_0^2 \pi}{2m\hbar} \sum_{k_1 k_2} \left(x_{k_1 k}y_{k_2 k} - x_{k_2 k}y_{k_1 k}\right)$$
$$\times \langle\Psi_{k_1}|\mathbf{\nabla}|\Psi_{k_2}\rangle t\delta(\Delta\omega). \quad \text{(B7)}$$

Here we emphasize the long-time conditions in the derivations of Eqs. (B6) and (B7). In real physical systems, due to the finite absorption linewidth γ_0, the condition for $t \to \infty$ in the previous mathematical limit will be weakened by the quantum uncertainty principle $t\Delta\omega \gg 1$. On the other hand, the time-dependent perturbation theory requires the small coefficient of the new eigenstates, i.e.,

$$\left|S_{k_1}(t)\langle\Psi_{k_1}|x + iy|\Psi_k\rangle\right|^2 \ll 1. \quad \text{(B8)}$$

It can be approximated as

$$t\delta(\Delta\omega)\frac{q^2 E_0^2 \pi}{2\hbar^2}\left(x_{k_1 k}^2 + y_{k_1 k}^2\right) \ll 1 \quad \text{(B9)}$$

in Eq. (6a). Therefore, there exists an effective range of time for the replacement of $S(t)$ by $\delta(\Delta\omega)$.

Then we use the basis transformation $|\Psi_k\rangle = \sum_n a_n^k|n\rangle$ to rewrite the transition and current formula from the molecular basis ($|\Psi_k\rangle$) to the atomic basis ($|n\rangle$). Here $\langle\Psi_k|\mathbf{\nabla}|\Psi_{k_1}\rangle$ in formulas above is written as

$$\langle\Psi_k|\mathbf{\nabla}|\Psi_{k_1}\rangle = \sum_{\langle n,n'\rangle} a_n^k a_{n'}^{k_1}\langle n|\mathbf{\nabla}|n'\rangle. \quad \text{(B10)}$$

In this summation only the nearest-neighbor basis vector $|n'\rangle$ for $\langle n|$ is calculated due to the local property of atomic basis. Substituting Eq. (B10) into Eqs. (B6) and (B7), we obtain

$$\mathbf{J}_{\text{type-II}} = \frac{q^2 E_0 \pi}{m} \sum_{\langle n,n'\rangle} \sum_{k_1} \left(x_{k_1 k}\cos\omega t + y_{k_1 k}\sin\omega t\right)$$
$$\times \left(a_n^k a_{n'}^{k_1} - a_n^{k_1} a_{n'}^k\right)\langle n|\mathbf{\nabla}|n'\rangle\delta(\Delta\omega), \quad \text{(B11)}$$

$$\mathbf{J}_{\text{type-III}} = \frac{q^3 E_0^2 \pi}{2m\hbar} \sum_{\langle n,n'\rangle} \sum_{k_1 k_2} \left(x_{k_1 k}y_{k_2 k} - x_{k_2 k}y_{k_1 k}\right)$$
$$\times a_n^{k_1} a_{n'}^{k_2}\langle n|\mathbf{\nabla}|n'\rangle t\delta(\Delta\omega). \quad \text{(B12)}$$

Finally, we rewrite Eqs. (B11) and (B12) in a summation form, i.e., $\mathbf{J}_{\text{type-II(III)}} = \sum_n \mathbf{J}_n^{\text{type-II(III)}}$. In other words, we di-

vide the "total" current vector into the "local" current vectors belonging to the region of each atom. So the formulas for local current at each atomic site n are obtained as shown in Eqs. (9a) and (9b).

When using Eqs. (9a) and (9b) for specific calculations, it involves the inner products of $\langle n|\mathbf{\nabla}|n'\rangle$ and $\langle n|x|n'\rangle$ ($\langle n|y|n'\rangle$). We use the Gaussian-type function to simulate the atomic orbitals in these GQD systems, i.e.,

$$|n\rangle = b_n\exp\left(\frac{-|\mathbf{r} - \mathbf{r_n}|^2}{\alpha^2}\right), \quad \text{(B13)}$$

where b_n and α are amplitude and localization parameter, $\mathbf{r}$ represents the electron position, and $\mathbf{r_n}$ represents the center of the nth atom in the GQD. It is easy to obtain

$$\langle n|\mathbf{\nabla}|n'\rangle = M(\mathbf{r_{n'}} - \mathbf{r_n}), \quad \text{(B14)}$$

$$\langle n|\mathbf{r}|n'\rangle = \mathbf{r_n}\delta_{nn'}. \quad \text{(B15)}$$

Namely, $\langle n|x|n'\rangle = x_n\delta_{nn'}$ and $\langle n|y|n'\rangle = y_n\delta_{nn'}$. The value of M in Eq. (B14) does not affect the main results of this work. Similar results can be found in the other work [48].

APPENDIX C: DERIVATION OF THE OPTICAL CONDUCTIVITY

We first utilize the operator commutation relation $\mathbf{\nabla} = \frac{m}{\hbar^2}[\mathbf{r}, H]$, where $\mathbf{\nabla}$ denotes the gradient operator, $\mathbf{r}$ represents the displacement vector operator, and H is the Hamiltonian, and we obtain

$$\langle\Psi_{k_1}|\mathbf{\nabla}|\Psi_k\rangle = \frac{m}{\hbar^2}\langle\Psi_{k_1}|[\mathbf{r}, H]|\Psi_k\rangle$$
$$= \frac{m(E_k - E_{k_1})}{\hbar^2}\langle\Psi_{k_1}|\mathbf{r}|\Psi_k\rangle. \quad \text{(C1)}$$

With the Fermi golden rule $(E_{k_1} - E_k = \hbar\omega)$, Eq. (C1) is simplified into

$$\langle\Psi_k|\mathbf{\nabla}|\Psi_{k_1}\rangle = -\langle\Psi_{k_1}|\mathbf{\nabla}|\Psi_k\rangle = \frac{m\omega}{\hbar}\langle\Psi_{k_1}|\mathbf{r}|\Psi_k\rangle. \quad \text{(C2)}$$

To obtain $\sigma(\omega)$, we start from the expression for the type-II current given in Eq. (20). Using Eq. (C2), we rewrite Eq. (20) in a vector form

$$\mathbf{J}_{\text{type-II}}$$
$$= \begin{bmatrix} j_x \\ j_y \end{bmatrix}$$
$$= \frac{2q^2 E_0 \pi\omega}{\hbar} \sum_{k_1} \left(x_{k_1 k}\cos\omega t + y_{k_1 k}\sin\omega t\right)\begin{bmatrix} x_{k_1 k} \\ y_{k_1 k} \end{bmatrix}\delta(\Delta\omega)$$
$$= \frac{2q^2 \pi\omega}{\hbar} \sum_{k_1} \begin{bmatrix} x_{k_1 k}^2 & y_{k_1 k}x_{k_1 k} \\ x_{k_1 k}y_{k_1 k} & y_{k_1 k}^2 \end{bmatrix}\begin{bmatrix} E_0\cos\omega t \\ E_0\sin\omega t \end{bmatrix}\delta(\Delta\omega). \quad \text{(C3)}$$

Here j_x and j_y are in-plane components of $\mathbf{J}_{\text{type-II}}$. We also have the definition of conductivity tensor [2]

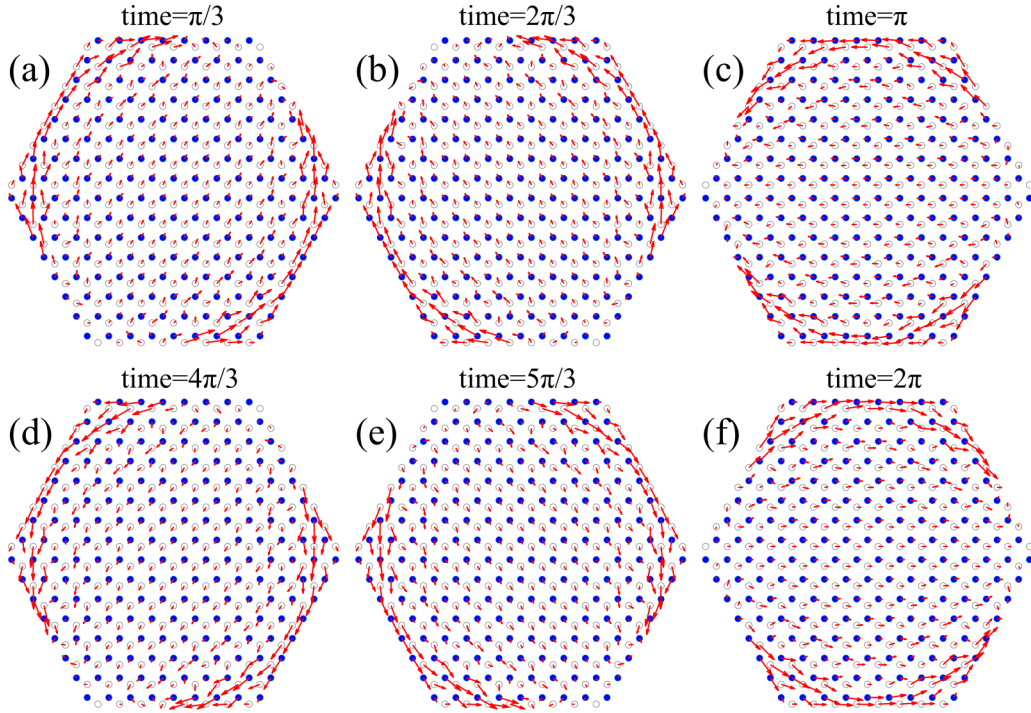$$j_\alpha = \sum_\beta \sigma_{\alpha\beta}(\omega)E_\beta, \quad \text{(C4)}$$

FIG. 11. The type-II local current distributions in larger-sized H-GQD ($N = 384$) under the CPL. [(a)–(f)] Snapshots in the period of light with the times (in unit $\frac{T}{2\pi}$) of $\frac{\pi}{3}$, $\frac{2\pi}{3}$, π, $\frac{4\pi}{3}$, $\frac{5\pi}{3}$, and 2π, respectively. The electron transition is from the HUMO to the LUMO levels.

where α and β represent x or y, respectively, and E_β represents the electric field component of the CPL. E_β can be written in a vector $\left[\begin{smallmatrix} E_0 \cos \omega t \\ E_0 \sin \omega t \end{smallmatrix}\right]$. So from Eq. (C3), we obtain the optical conductivity tensor for the photoinduced type-II current

$$\sigma_{\alpha\beta}(\omega) = \frac{2q^2\pi\omega}{\hbar} \sum_{k_1} \begin{bmatrix} x_{k_1k}^2 & y_{k_1k}x_{k_1k} \\ x_{k_1k}y_{k_1k} & y_{k_1k}^2 \end{bmatrix} \delta(\Delta\omega). \quad \text{(C5)}$$

In this study, we focus mainly on the intrinsic properties of the material, assuming the system to be isotropic. It suffices to consider only the diagonal elements of the optical conductivity tensor [2]. This assumption leads to Eq. (C6) for a scalar conductivity by tracing the matrix in Eq. (C5)

$$\sigma_0(\omega) = \frac{2q^2\pi\omega}{\hbar} \sum_{k_1} \text{Tr} \begin{bmatrix} x_{k_1k}^2 & y_{k_1k}x_{k_1k} \\ x_{k_1k}y_{k_1k} & y_{k_1k}^2 \end{bmatrix} \delta(\Delta\omega)$$

$$= \frac{2q^2\pi\omega}{\hbar} \sum_{k_1} (x_{k_1k}^2 + y_{k_1k}^2)\delta(\Delta\omega). \quad \text{(C6)}$$

Moreover, as the electrons follow the Fermi-Dirac distribution, by summating all possible initial and final states in the optical transitions, the optical conductivity per unit area can be expressed as

$$\sigma(\omega) = \frac{2\pi q^2\omega}{A\hbar} \sum_{k_1k} |\langle \Psi_{k_1}|x + iy|\Psi_k\rangle|^2$$

$$\times [f(E_k) - f(E_{k_1})]\delta(\Delta\omega). \quad \text{(C7)}$$

Equation (C7) is identical with the optical conductivity formula of Eq. (10a).

APPENDIX D: PHOTOINDUCED CURRENTS IN LARGE-SIZED GQDs

Here, using Eq. (9), we calculate both type-II and type-III currents for a H-GQD with $N = 384$, and type-III current for a T-GQD with $N = 321$, where electrons transition from the HUMO to the LUMO levels under the CPL radiation. These currents are displayed in Fig. 11 (type-II) and Fig. 12 (type-III).

The characteristics of these type-II dynamic currents and type-III quasisteady rotational currents are akin to those observed in smaller GQDs (as illustrated in Figs. 2 and 3). But for the large-sized H-GQD, when the transition-related eigenstates have the near-zero eigenvalues (we usually use the HOMO and the LUMO, with eigenenergies of $\pm 0.048t$), the photoinduced currents are mainly distributed on the boundaries of the GQD. This is because the eigenstates of HOMO and LUMO also have the edge-state property due to their
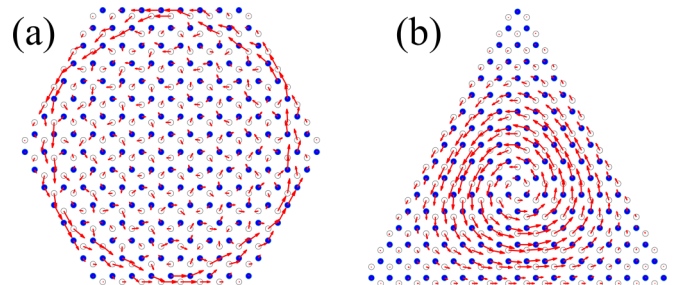

FIG. 12. The type-III steady local current distributions in larger-sized H-GQD ($N = 384$) and T-GQD ($N = 321$) under the CPL. The electron transition is from the HUMO to the LUMO levels.
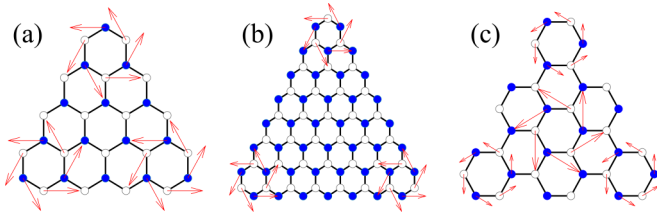
FIG. 13. The type-III current distributions for three specific T-GQDs at the photon energy of $\hbar\omega = 2t$ with circular polarization. (a) T-GQD with zigzag edges ($N = 33$), (b) T-GQD with zigzag edges ($N = 78$), (c) T-GQD with armchair edges ($N = 36$).

near-zero eigenvalues. Since the currents are related to the eigenstates (see Eq. (8c)), the currents may also flow near the edges of GQD.

For the large-sized T-GQD, we find that the HOMO and LUMO are not very close to zero ($\pm 0.329t$). So these eigenstates and the corresponding photoinduced type-III currents are not on the edges of GQD but in the center.

APPENDIX E: CORNER MAGNETIC MOMENTS OF T-GQD

For different degenerate excited states, the type-III current does not always rotate around the center of the GQD, i.e., there also exist some different distributions of magnetic moments, as shown in Fig. 13 below.

In the tight-binding Hamiltonian H_0, all GQDs have the electronic states with energies of $\pm t$ due to the symmetry,

similar to the Van Hove singularities in bulk graphene [28,49]. The number of these states depends on the size, shape, and edge type of the GQD. In the T-GQD with a zigzag edge, these states always exist regardless of the size and they are degenerate. On the other hand, the absorption peak corresponding to the electronic transition $\hbar\omega = 2t$ in the absorption spectrum always exist which means this optical transition obeys the selection rule [2,49].

Here we present a special distribution of magnetic moments in T-GQD with a zigzag edge. They result from the transitions from the energy levels $-t$ to t by the CPL radiation, as seen in Fig. 13.

As we see, the rotating currents in two different sizes of zigzag T-GQD only appear locally at the three corners. In this way, the magnetic moment distribution is also on these three corners. Furthermore, for these T-GQDs, it can be found that the GQD size does not affect the magnetic moment distribution.

In Fig. 13(c), we also illustrate the type-III current distribution for a T-GQD with armchair edges. We observe that besides the three corner magnetic moments, there is still one magnetic moment positioned in the center of this GQD. This is different from the previous distributions.

These magnetic moments all can generate magnetic fields in the same direction. However, this type of novel IFE has not been reported in the GQD system before. We believe these interesting magnetic features can be detected in future experiments on large zigzag-edge or armchair-edge T-GQDs.

[1] I. Ozfidan, A. D. Guclu, M. Korkusinski, and P. Hawrylak, Phys. Status Solidi RRL **10**, 102 (2016).

[2] R. Pohle, E. G. Kavousanaki, K. M. Dani, and N. Shannon, Phys. Rev. B **97**, 115404 (2018).

[3] Y. Yan, J. Gong, J. Chen, Z. Zeng, W. Huang, K. Pu, J. Liu, and P. Chen, Adv. Mater. **31**, 1808283 (2019).

[4] F. Qi and G. Jin, J. Appl. Phys. **114**, 073509 (2013).

[5] Y. Wang, G. Yu, M. Rosner, M. I. Katsnelson, H.-Q. Lin, and S. Yuan, Phys. Rev. X **12**, 021055 (2022).

[6] Q.-R. Dong, Y. Li, C. Jia, F.-L. Wang, Y.-T. Zhang, and C.-X. Liu, Solid State Commun. **273**, 55 (2018).

[7] Q.-R. Dong and C.-X. Liu, RSC Adv. **7**, 22771 (2017).

[8] E. G. Kavousanaki and K. M. Dani, Phys. Rev. B **91**, 035433 (2015).

[9] D. Xiao, G.-B. Liu, W. Feng, X. Xu, and W. Yao, Phys. Rev. Lett. **108**, 196802 (2012).

[10] G. F. Quinteiro and T. Kuhn, Phys. Rev. B **90**, 115401 (2014).

[11] A. Steiger and C. Woods, Phys. Rev. A **5**, 1467 (1972).

[12] V. Karakhanyan, C. Eustache, Y. Lefier, and T. Grosjean, Phys. Rev. B **105**, 045406 (2022).

[13] S. Ali, J. R. Davies, and J. T. Mendonca, Phys. Rev. Lett. **105**, 035001 (2010).

[14] T. V. Liseykina, S. V. Popruzhenko, and A. Macchi, New J. Phys. **18**, 072001 (2016).

[15] Y. Mou, X. Yang, B. Gallas, and M. Mivelle, Nanophotonics **12**, 2115 (2023).

[16] X. Yang, Y. Mou, R. Zapata, B. Reynier, B. Gallas, and M. Mivelle, Nanophotonics **12**, 687 (2023).

[17] M. Battiato, G. Barbalinardo, and P. M. Oppeneer, Phys. Rev. B **89**, 014413 (2014).

[18] S. Abedi and A. Hamed Majedi, J. Phys. B **56**, 145502 (2023).

[19] I. D. Tokman, Q. Chen, I. A. Shereshevsky, V. I. Pozdnyakova, I. Oladyshkin, M. Tokman, and A. Belyanin, Phys. Rev. B **101**, 174429 (2020).

[20] S. O. Potashin, V. Y. Kachorovskii, and M. S. Shur, Phys. Rev. B **102**, 085402 (2020).

[21] S. Banerjee, U. Kumar, and S.-Z. Lin, Phys. Rev. B **105**, L180414 (2022).

[22] A. H. Majedi and B. Lounis, Phys. Rev. B **102**, 214401 (2020).

[23] H. Hsu and L. E. Reichl, Phys. Rev. B **76**, 045418 (2007).

[24] S. R. Tauchert, M. Volkov, D. Ehberger, D. Kazenwadel, M. Evers, H. Lange, A. Donges, A. Book, W. Kreuzpaintner, U. Nowak, and P. Baum, Nature (Lond.) **602**, 73 (2022).

[25] H. Zhu, J. Yi, M.-Y. Li, J. Xiao, L. Zhang, C.-W. Yang, R. A. Kaindl, L.-J. Li, Y. Wang, and X. Zhang, Science **359**, 579 (2018).

[26] P. R. Wallace, Phys. Rev. **71**, 622 (1947).

[27] S. Reich, J. Maultzsch, C. Thomsen, and P. Ordejón, Phys. Rev. B **66**, 035412 (2002).

[28] A. H. Castro Neto, F. Guinea, N. M. R. Peres, K. S. Novoselov, and A. K. Geim, Rev. Mod. Phys. **81**, 109 (2009).

[29] S. Bougouffa and M. Babiker, Phys. Rev. A **102**, 063706 (2020).

[30] G. F. Quinteiro, D. E. Reiter, and T. Kuhn, Phys. Rev. A **91**, 033808 (2015).

[31] K. Nobusada and K. Yabana, Phys. Rev. A **75**, 032518 (2007).

[32] D. J.Griffiths, *Introduction to Quantum Mechanics* (Addison-Wesley, Boston, MA, 2005).

[33] A. Altıntaş, K. E. Çakmak, and A. D. Güçlü, Phys. Rev. B **95**, 045431 (2017).

[34] T. Basak, T. Basak, and A. Shukla, Phys. Rev. B **103**, 235420 (2021).

[35] V. N. Kotov, B. Uchoa, V. M. Pereira, F. Guinea, and A. H. Castro Neto, Rev. Mod. Phys. **84**, 1067 (2012).

[36] A. D. Güçlü, P. Potasz, and P. Hawrylak, Phys. Rev. B **82**, 155445 (2010).

[37] N. Mohanty, D. Moore, Z. Xu, T. S. Sreeprasad, A. Nagaraja, A. A. Rodriguez, and V. Berry, Nat. Commun. **3**, 844 (2012).

[38] L. Allen, M. W. Beijersbergen, R. J. C. Spreeuw, and J. P. Woerdman, Phys. Rev. A **45**, 8185 (1992).

[39] H. F. Jones, *Groups, Representations, and Physics* (IOP Publishing, Bristol, 1998).

[40] J. Zhou, H. Li, Z. Yang, Z. Zhang, X. Shen, and K. Han, Carbon Trends **4**, 100054 (2021).

[41] D. Mombrú, M. Romero, R. Faccio, and A. W. Mombrú, Appl. Surf. Sci. **462**, 540 (2018).

[42] L. V. Dzemiantsova, M. Karolak, F. Lofink, A. Kubetzka, B. Sachs, K. von Bergmann, S. Hankemeier, T. O. Wehling, R. Frömter, H. P. Oepen, A. I. Lichtenstein, and R. Wiesendanger, Phys. Rev. B **84**, 205431 (2011).

[43] S. Yoshida, Y. Aizawa, Z.-h. Wang, R. Oshima, Y. Mera, E. Matsuyama, H. Oigawa, O. Takeuchi, and H. Shigekawa, Nat. Nanotechnol. **9**, 588 (2014).

[44] L. Zhang and Q. Niu, Phys. Rev. Lett. **115**, 115502 (2015).

[45] A. Einstein and W. J. de Haas, Verh. Dtsch. Phys. Ges. **17**, 152 (1915).

[46] R. A. Beth, Phys. Rev. **50**, 115 (1936).

[47] J. H. Mentink, M. I. Katsnelson, and M. Lemeshko, Phys. Rev. B **99**, 064428 (2019).

[48] H. Abdelsalam, M. H. Talaat, I. Lukyanchuk, M. E. Portnoi, and V. A. Saroka, J. Appl. Phys. **120**, 014304 (2016).

[49] A. Zhou and W. Sheng, J. Appl. Phys. **112**, 094313 (2012).